ROYAL SOCIETY
OF CHEMISTRY

# Facile and robust hybrid TENG for harvesting wind energy and water flow energy

Jiaxi Hu, [ab] Mengfan Li, [ID] [bc] Ying Lou, [ab] Weiqi Cui, [ab] Jiaodi Li, [ab] Qiuxiang Wang, [ab] Aifang Yu*[abc] and Junyi Zhai [ID] *[abc]

The ocean contains a vast source of energy, and triboelectric nanogenerators (TENGs) are emerging as a promising technology for its harvesting. Here, we report a facile-fabricated, robust hybrid TENG (H-TENG) designed to simultaneously harvest wind and water flow energy. The device, fabricated using 3D and electronic design automation (EDA) technologies, comprises an upper wind-driven unit (WH-TENG) and a lower water flow-driven unit (WFH-TENG). WH-TENG utilizes rabbit fur to achieve a high short-circuit current ($I_{sc}$) of 14.8 μA and a peak power of 3.54 mW, demonstrating exceptional durability by retaining 92% of its initial charge transfer (130.9 nC) after seven weeks. WFH-TENG, designed for simple preparation and integration, delivers a peak power of 1.13 mW. As a practical application, the integrated H-TENG successfully powers a water level alarm within 150 s. This work demonstrates a viable strategy for multi-energy harvesting in marine environments, paving the way for the long-term and comprehensive utilization of ocean energy.

## 1. Introduction

The oceans provide humanity with essential natural resources, like food and medicine, while helping protect coastal ecosystems from harsh natural conditions.[1,2] Deploying a large network of ocean sensors enables real-time, on-site ocean condition monitoring, providing crucial data for marine conservation and scientific research. Traditional sensors, however, are limited by the lifespan of their batteries, which are costly and labor-intensive to replace.[3] Given the abundance of wind,[4,5] solar,[6,7] water flow,[8–10] and wave energy[11,12] in the marine environment, developing a technology that captures energy from these sources offers a promising solution.

Since its first report in 2012,[13] TENGs have been widely used to convert mechanical energy, such as wind,[14–18] sound,[19,20] waves,[21,22] human movement[23,24] and mechanical vibration,[25] into electrical energy. TENGs can also be used for gas detection.[26–29] Due to their broad material compatibility, low production costs,[30] flexible sizing,[31] and high efficiency in capturing low-frequency energy, TENGs are better suited for the

marine environment to harvest energy. Various configurations of TENGs have been designed over the past decade to optimize water wave energy capture. For instance, a spherical TENG configuration was used to harness water-wave energy, and Qu *et al.* integrated multiple TENG units within a sphere housing to maximize the space utilization and achieve a high power density.[32] Xu *et al.* combined two distinct TENG units, allowing the device to effectively capture wave energy under both small and large wave conditions.[33]

Despite extensive research on the effective extraction of water wave energy, research on harnessing the ocean's vast wind energy resources remains largely unexplored. Xi *et al.* designed a hybrid TENG to capture multiple ocean energy sources,[34] but this design relied on an etching process to boost output, adding complexity to the fabrication of TENG. In fact, some other measures can also be implemented to improve the surface charge density of TENG,[35–37] although such methods will increase manufacturing complexity. Moreover, scaling up H-TENG production and ensuring its stability for deployment across the vast ocean pose pressing challenges.

To better harness ambient energy, we designed an H-TENG for harvesting both wind and water flow energy based on an independent layer motion model. First, we significantly shortened the charge-transfer ($Q_{sc}$) time by reducing the WH-TENG electrode sector angle, thereby substantially increasing the $I_{sc}$ to 14.8 μA. Second, by employing rabbit fur and a non-contact structure, WH-TENG still transfers a $Q_{sc}$ of 130.9 nC after a long period of time, which is 92% of the initial value. WFH-TENG also achieved a high $I_{sc}$ by reducing the electrode width. These two types of TENGs have greatly reduced the

*aCenter on Nanoenergy Research, Institute of Science and Technology for Carbon Peak & Neutrality, Key Laboratory of Blue Energy and Systems Integration (Guangxi University), Education Department of Guangxi Zhuang Autonomous Region, School of Physical Science & Technology, Guangxi University, Nanning 530004, China*

*bBeijing Key Laboratory of Micro-Nano Energy and Sensor, Center for High-Entropy Energy and Systems, Beijing Institute of Nanoenergy and Nanosystems, Chinese Academy of Sciences, Beijing 101400, P. R. China. E-mail: yuaifang@binn.cas.cn; jyzhai@binn.cas.cn*

*cSchool of Nanoscience and Engineering, University of Chinese Academy of Science, Beijing 100049, China*

manufacturing time of TENGs due to the introduction of 3D printing technology and EDA technology. With the addition of an energy management circuit (EMC), the time required for H-TENG to reach the target voltage is greatly reduced. Finally, we realized the continuous operation of two thermo-hygrometers and the activation of the water level alarm device within 150 s.

## 2. Results and discussion

### 2.1 Structural design and operating principle of H-TENG

H-TENG is a dual-component system for simultaneous energy harvesting, comprising a WH-TENG in the upper section and a WFH-TENG in the lower section. Fig. 1 illustrates the integrated structure and operating principle of H-TENG, with decomposed views of its components provided in Fig. S1. Fig. S1a details WH-TENG, while Fig. S1b presents the design of WFH-TENG.

The three-dimensional assembly of H-TENG is shown in Fig. 1a. In the upper section, horizontal airflow converges on the concave surfaces of the wind cup, inducing a counterclockwise rotation. This rotational motion is transferred to a rotor,

enabling WH-TENG to generate electrical energy *via* a free-standing triboelectric mode. In the lower section, a horizontal water flow drives nearly vertical turbine blades. These blades rotate around a central steel rod, transferring kinetic energy to a rotor. A crown gear mechanism then converts this horizontal rotation into a vertical linear displacement, which allows WFH-TENG to generate electricity. Cross-sectional views of WH-TENG and WFH-TENG are presented in Fig. 1b and c, respectively.

WFH-TENG harvests energy from ocean currents, while WH-TENG captures wind energy. While ocean energy research has predominantly focused on wave power, significant potential also lies in water flow energy. Crucially, the presence of waves often correlates with available wind energy, a resource that is frequently overlooked. This H-TENG design provides an integrated solution by simultaneously harnessing energy from both ocean currents and wind, thereby maximizing energy collection efficiency in marine environments. To validate the hybrid design and output characteristics of H-TENG, we compared multiple triboelectric nanogenerators (see SI Table S1), conducting a comprehensive evaluation encompassing modes,
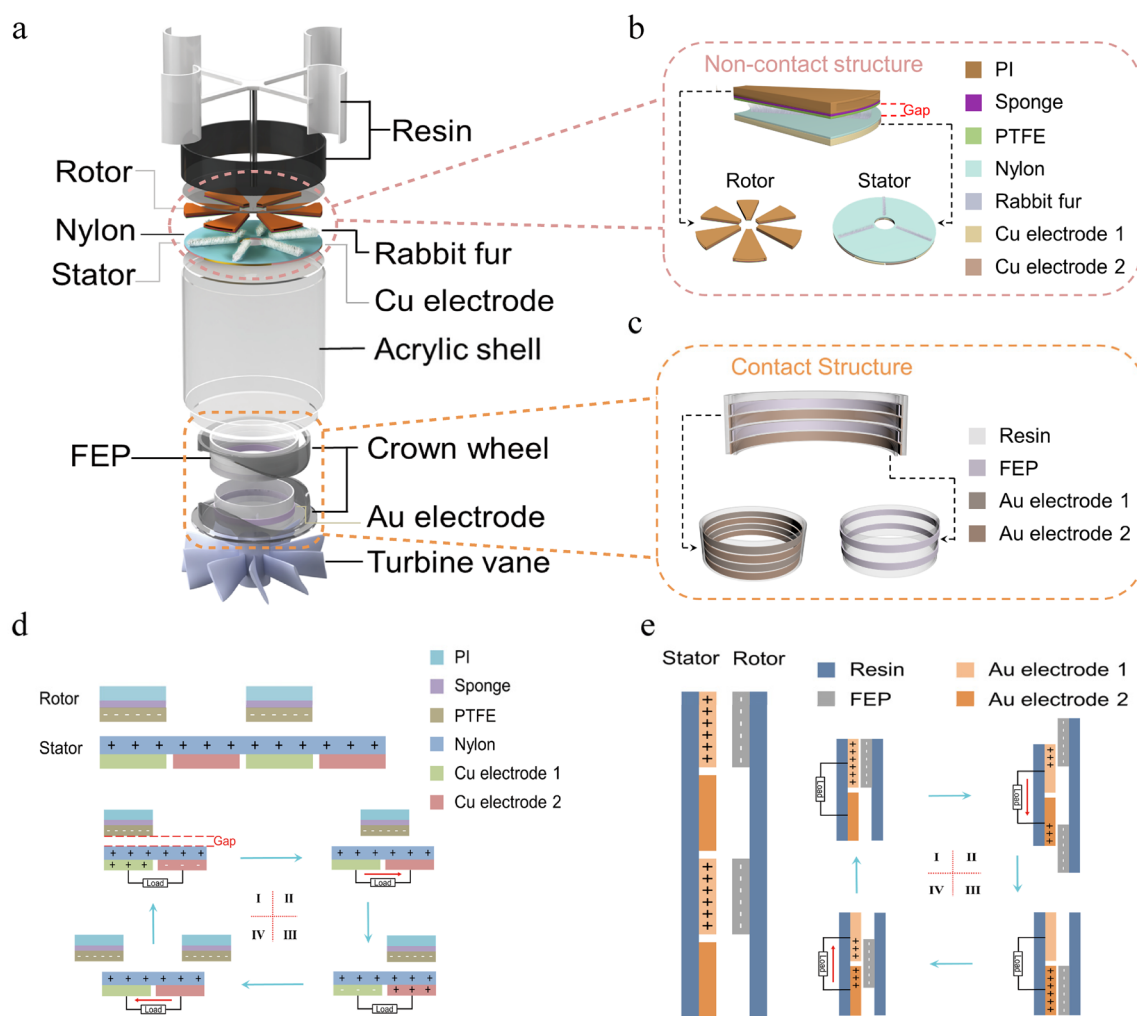


Fig. 1 Working principle and structural design of H-TENG. (a) Three-dimensional schematic of H-TENG. (b) Cross-sectional view of WH-TENG. (c) Cross-sectional view of WFH-TENG. (d) Operational mechanism of WH-TENG during a single motion cycle. (e) Operational mechanism of WFH-TENG during a single motion cycle.

designs, working mechanisms, energy sources, contact modes, electrode fabrication modes, and outputs. Through ingenious hybrid design, TENG enables hybrid harvesting of diverse energy sources while offering novel insights for designing new hybrid triboelectric nanogenerators.

WH-TENG has two key components: a wind-capturing turbine and a TENG unit that converts this energy into electricity. The turbine transforms ambient wind energy into rotational mechanical energy. Unlike traditional hemispherical wind cups, which require a proportional increase in overall size to achieve a larger windward cross-sectional area, our design adopts a semi-cylindrical shape. This geometry, inspired by vertical-axis wind turbines, allows for a maximized cross-sectional area by extending the vertical dimension while maintaining a compact horizontal footprint. To minimize rotational friction, the central shaft of the turbine is equipped with low-resistance R688 ceramic bearings, which are specifically optimized for high-speed operation.

The performance of wind-energy harvesters is influenced by air density, which is positively correlated with aerodynamic forces. Lower air density reduces these forces, a condition under which horizontal-axis harvesting strategies prove particularly effective. WH-TENG's core triboelectric components are structured as follows: on the rotor, a ring support made of polyimide (PI) film is fitted at intervals, with a thin sponge layer coated in polytetrafluoroethylene (PTFE) film affixed. The stator features complementary copper grid electrodes covered by a thin nylon film, with three equally spaced rabbit fur patches attached. This design minimizes operational friction and material wear without compromising charge-transfer efficiency, enabling functionality at low wind speeds.

The working principle of WH-TENG over a single motion cycle is illustrated in Fig. 1d(I–IV), centering on the contact-electrification of PTFE and the subsequent electrostatic induction. Initially, friction between the PTFE-coated rotor and the rabbit fur on the stator charges the PTFE surface negatively. As shown in Fig. S2, a newly fabricated WH-TENG exhibits a low $Q_{sc}$ of 125 nC, as the PTFE surface charge is minimal. However, after a 30-minute continuous break-in period, the $Q_{sc}$ stabilizes at approximately 267 nC. In the initial state (Fig. 1d-I), the negatively charged PTFE overlaps with the left copper electrode (Electrode 1), inducing a positive charge on it. As the rotor turns, the PTFE moves toward the right electrode (Electrode 2). This movement drives electrons from the right electrode to the left through the external circuit to balance the electrostatic potential (Fig. 1d-II). When the PTFE fully overlaps with the right electrode, the positive charge on this electrode is maximized, creating the peak potential difference between the two electrodes (Fig. 1d-III). In the fourth stage, as rotation continues, the PTFE moves away, causing electrons to flow in the reverse direction, returning the system to its initial state. This back-and-forth electron flow generates an alternating current (AC) in the external circuit.

The operating principle of WFH-TENG illustrated in Fig. 1e(I–IV) is fundamentally similar to that of WH-TENG. The primary distinction lies in its triboelectric pair: fluorinated ethylene propylene (FEP) acquires a negative charge through contact with a gold (Au) layer. To enhance the charge-transfer efficiency, FEP was selected over PTFE owing to its higher electron affinity. To optimize device performance, we systematically investigated how key parameters affect the WH-TENG's electrical output, including contact methods, fan-shaped electrode central angle, friction materials, and wind speed.

For WFH-TENG, however, experimental design was more complex. The interdependence between the pump's water flow rate and pressure meant that varying one parameter inherently affected the other, making it difficult to isolate their individual effects. Consequently, the investigation for WFH-TENG was narrowed to focus exclusively on the influence of the Au electrode width and the TENG unit length on its output performance.

## 2.2 Output performance of WH-TENG under varying parameters

The electrical output of WH-TENG was systematically evaluated by varying the contact structure, electrode central angle, and triboelectric materials, with the results summarized in Fig. 2. A photograph of the assembled device is presented in Fig. 2a. To enhance long-term durability and reduce maintenance, we designed and compared four distinct TENG structures, tested at a fixed electrode central angle of 60° and wind speed of approximately 7 m s$^{-1}$ (Fig. 2b). The rotor structure shown in Fig. 2b-i employs a sandwich configuration, consisting of an inner PI film layer, a middle sponge layer, and an outer PTFE film. This design leverages the low friction coefficient and self-lubricating properties of PTFE, combined with the elasticity of the PI film, to significantly reduce operational friction. The resulting reduction in wear not only improves device longevity but also facilitates easier start-up and enhances overall performance. As shown in Fig. 2b-ii, the PI film is formed into a ring with a thin sponge layer beneath the PTFE film. This assembly generates a relatively uniform downward force on the stator, ensuring consistent, slight contact between the PTFE and nylon layers. The contact quality of the structure in Fig. 2b-i is superior to that of Fig. 2b-ii, due to the higher elasticity of the PI film, resulting in a slightly higher $Q_{sc}$. The rotor design in Fig. 2b-iii is similar to that of Fig. 2b-ii, but features a non-contact mode with an approximately 3 mm gap maintained between the PTFE and nylon layers. This design minimizes frictional resistance but requires rabbit fur pre-treatment of the PTFE surface to initiate triboelectric charging. Leveraging PTFE's excellent charge-retention capability, the $Q_{sc}$ for structure III exceeds those for structures I and II, attributed to the superior electron-donating ability of rabbit fur compared to that of nylon. The rotor in Fig. 2b-iv is identical to that in structure iii, with the key addition being a rabbit fur layer integrated into the stator. This modification eliminates the need for external pre-treatment, as the PTFE surface charge is continuously replenished through consistent friction with the rabbit fur. Consequently, this configuration achieves a significantly higher $Q_{sc}$ of 274 nC. Furthermore, it maintains low overall frictional resistance, as the PTFE contacts only the low-friction tips of the rabbit fur.

The influence of the electrode's central angle was also investigated. As this angle decreases, $I_{sc}$ progressively increases
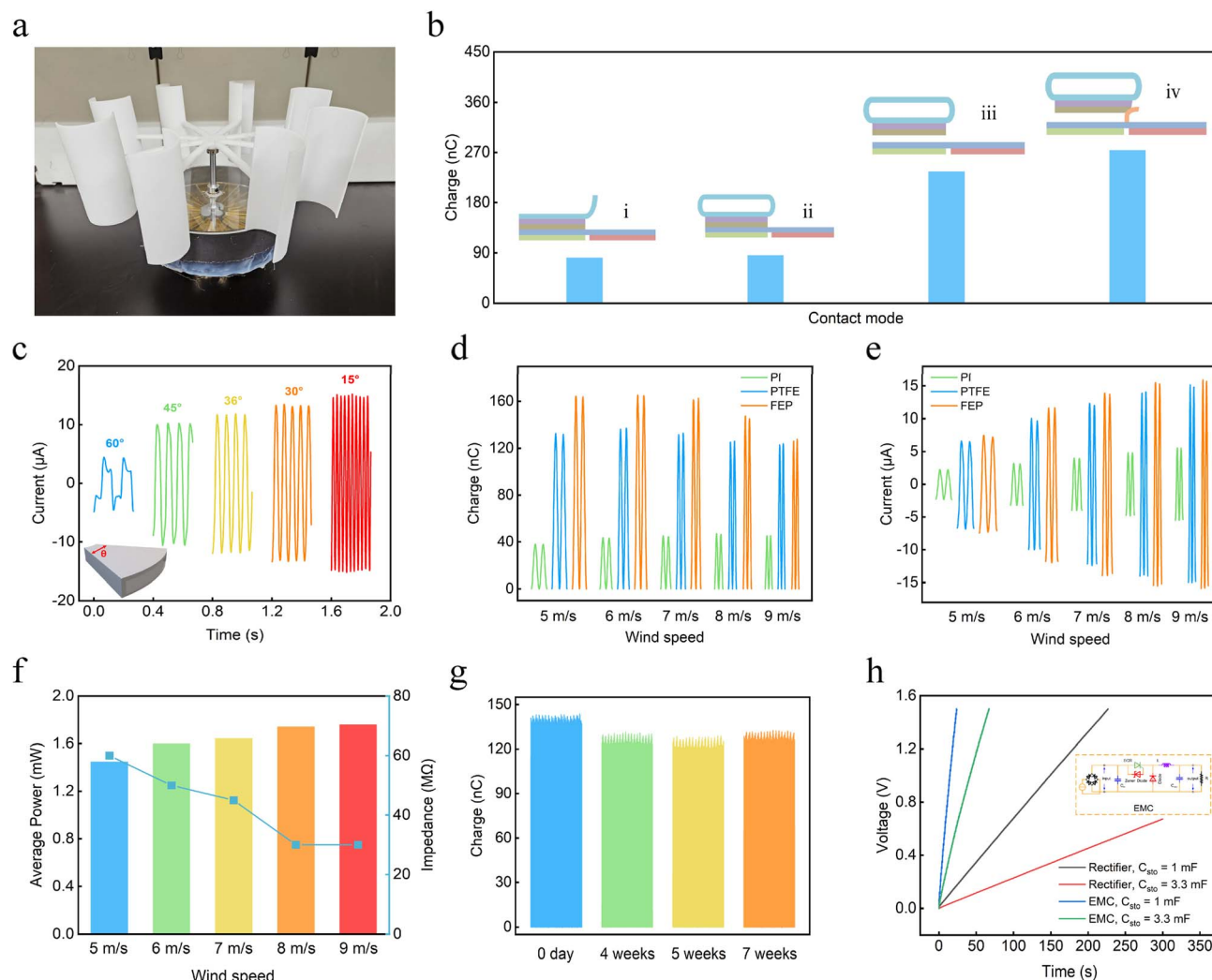
Fig. 2 Electrical output of WH-TENG under various parameters. (a) Photograph of the assembled WH-TENG. (b) Impact of different contact structures on the $Q_{sc}$ of WH-TENG. (c) Output current of WH-TENG at varying electrode angles. (d and e) Influence of different materials on the output of WH-TENG. (f) Output of WH-TENG across different wind speeds. (g) Changes in the $Q_{sc}$ of WH-TENG after being placed for a period of time. (h) Comparison of the charging curves for 1 mF and 3.3 mF capacitors using an EMC and rectifier bridge.

from 4.3 μA to 14.7 μA (Fig. 2c), while the operating frequency rises from 7.5 Hz to 38.9 Hz (Fig. S3). The reduction in the central angle increases the charge-transfer rate per rotor rotation, leading to a higher $I_{sc}$. The reduction in the center-of-circle angle enhances the charge-transfer rate during each complete rotation of the rotor, leading to an increase in current, as expressed by eqn (1), where $\Delta Q$ represents the amount of $Q_{sc}$ between nylon and PTFE:

$$I = \frac{\Delta Q}{\Delta t} \qquad (1)$$

The amount of $Q_{sc}$ during triboelectric contact is governed by the electron affinity of the constituent materials. In this study, three electron-negative materials—PI, PTFE, and FEP—were evaluated as cathode materials to determine their impact on the output performance. As shown in Fig. 2d and e, both $Q_{sc}$ and $I_{sc}$ increased with the material's electronegativity, following the trend PI < PTFE < FEP. PI, with fewer fluorine groups in its

molecular structure, exhibits the weakest electron affinity, leading to the lowest $Q_{sc}$. In contrast, PTFE and FEP possess a similar density of fluorine groups, resulting in comparable $Q_{sc}$ and $I_{sc}$ values at identical wind speeds. Although FEP's $Q_{sc}$ fluctuated slightly with wind speed, PTFE demonstrated superior output stability. Furthermore, PTFE offers advantageous properties, such as self-lubrication and a low coefficient of friction. Based on this comprehensive analysis, PTFE was selected as the optimal tribo-negative material to ensure stable performance and durability.

Under the selected conditions—a 15° central electrode angle and a wind speed of 9 m s$^{-1}$—WH-TENG achieved an $I_{sc}$ of 14.8 μA and a $Q_{sc}$ of 123 nC.

We denote the height of the wind cup rotation axis as $h$ and the length of the wind cup support as $L$. Assuming that the position $\theta_i$ of the wind cup numbered $i$ in the $x$–$y$ coordinate plane in the polar coordinate system can be expressed as eqn

(2), then its position $r_i$ in the cartesian coordinate system can be expressed as eqn (3):

$$\theta_i = i \cdot 45° \quad (i = 0, 1, \ldots, 7) \tag{2}$$

$$r_i = (L \cos \theta_i, L \sin \theta_i, h) \quad (i = 0, 1, \ldots, 7) \tag{3}$$

The projected area of the wind cup is denoted as $A$; the drag coefficients of the concave and convex surfaces of the wind cup are denoted as $C_{d_1}$ and $C_{d_2}$, respectively, and the damping coefficient of the system is denoted as $b$. When the external wind speed is $v$, according to the drag equation, we can get the drag force of the wind cup with the number of $i$ as in eqn (4), where $\rho$ is the density of air:

$$F_i = \frac{1}{2} \rho A C_d v^2 \tag{4}$$

The drive torque ($\tau_{drive}$) of WH-TENG can be derived from eqn (5):

$$\tau_{drive} \approx 4 \cdot \frac{1}{2} \rho A v^2 L (C_{d_1} \cdot \sin(45°) - C_{d_2} \cdot \sin(135°))$$
$$= \sqrt{2} \rho A L (C_{d_1} - C_{d_2})(v - \omega L)^2 \tag{5}$$

The damping torque ($\tau_{damping}$) originates from air resistance against the acrylic plate, rotational resistance generated by bearing friction during shaft rotation, and friction between PTFE and rabbit fur. Since it is related to the angular velocity, it can be approximated as expressed in eqn (6), where $b$ is the damping coefficient.

$$\tau_{damping} = b\omega \tag{6}$$

The difference between the driving torque and the resisting torque drives the disk to rotate:

$$\frac{1}{2} m R^2 \frac{d\omega}{dt} = \sqrt{2} \rho A L (C_{d_1} - C_{d_2})(v - \omega L)^2 - b\omega \tag{7}$$

Then, we can easily obtain the TENG rotational angular velocity $\omega$ at steady state, as expressed in eqn (8):

$$\omega = \frac{v}{L} + \frac{b + \sqrt{b(b + 4\sqrt{2} \rho A L^2 (C_{d_1} - C_{d_2})v)}}{2\sqrt{2} \rho A L^3 (C_{d_1} - C_{d_2})} \tag{8}$$

Since the overlap area between PTFE and nylon at time $t$ is proportional to the result of $\omega \times t$, we denote this coefficient as $k$ and the surface charge density of the material as $\sigma$. Then, the relationship between the current $I$ and $\omega$ is shown in eqn (9):

$$I = \frac{dQ}{dt} = \sigma \times k \times \omega \tag{9}$$

The current $I$ is proportional to $\omega$ since both $\sigma$ and $k$ are constant, and therefore, $I_{sc}$ is proportional to the outside wind speed. Therefore, the $I_{sc}$ of WH-TENG can be increased by increasing the outside wind speed.

The output power of WH-TENG as a function of wind speed is presented in Fig. 2f. As wind speed increases, $I_{sc}$ increases, but $Q_{sc}$ and $V_{oc}$ remain unchanged (Fig. S4a–c). The average power rose to 1.76 mW (Fig. S4d), with a maximum peak power of 3.54 mW (Fig. S4e). Concurrently, the optimal load impedance decreased from 60 MΩ to 30 MΩ. Theoretically, the open-circuit voltage ($V_{oc}$) should remain largely unaffected by the wind speed, as it peaks only at full electrode overlap. Experimental results confirm this, with the $V_{oc}$ maintaining a stable value of approximately 1 kV (Fig. S4b). To investigate the structural stability and performance of WH-TENG, a 15 000 s cycling test was conducted, as shown in Fig. S5 (SI). Fig. S5a(i–iii) (SI) displays the actual data of WH-TENG after cycling at 1, 2, and 3 hours, respectively. The long-term stability test demonstrates that the current value of WH-TENG remains unchanged, fully proving the outstanding operational stability of the non-contact structure. The observed increase in power with wind speed at a nearly constant voltage is therefore attributed to the reduction in matching impedance. This indicates that higher wind speeds result in an increased charge-transfer rate, effectively lowering the internal impedance. This inverse relationship between optimal impedance and wind speed was consistently observed across various electrode angles ($\theta = 30°$, $36°$, $45°$, and $60°$), as illustrated in Fig. S6.

Our fabricated WH-TENG employs a non-contact mode to minimize operational friction, whereas conventional TENGs often rely on a contact-separation mode, where higher output is achieved at the expense of increased friction. As shown in Fig. 2g, WH-TENG's $Q_{sc}$ reached 142.8 nC immediately after fabrication and retained 92% of its initial value after 7 weeks, demonstrating excellent long-term durability. This robust performance is attributed to two key factors: the superior charge retention capability of PTFE and the continuous surface charge replenishment from the slight contact with the rabbit fur. To further assess wear, the PTFE surface was examined under light microscopy after extended operation (Fig. S7). Apart from minor air bubbles introduced during manufacturing, the surface showed no significant friction marks, confirming that the non-contact design successfully achieves both low wear and high electrical output.

The TENG exhibits AC output characterized by high voltage and low current, primarily due to its very high matching impedance (typically tens to hundreds of MΩ). However, common electronic devices, such as thermo-hygrometers, operate at low voltages and require high currents, making it impractical to directly power such devices using the TENG. A simple DC–DC buck circuit is shown in Fig. S8, which serves as a foundation for constructing an EMC tailored to the TENG. The circuit incorporates a small high-voltage-tolerant capacitor ($C_{in}$), a silicon-controlled rectifier (SCR), and a voltage regulator diode, enabling automatic switching of the transistor within the buck circuit. The EMC we designed for WH-TENG is shown in Fig. S9a, and its operation process consists of four stages. The parameters of the circuit components are detailed in Fig. S9b–d. Fig. S9b illustrates the basis for selecting the $C_{in}$ capacitor. Fig. S9c presents the impact of different breakdown voltages of voltage regulator diodes on the voltage across the energy storage

capacitor ($C_{sto}$). Fig. S9d shows that the inductance value of the EMC circuit is unaffected by the capacitance value of $C_{sto}$. This finding indicates that an appropriate $C_{sto}$ can be selected based on the requirements of the electronic device, without adjusting the inductor size in the circuit. Fig. S9e shows an interesting phenomenon we found in our tests: when varying the size of the inductor, the $C_{sto}$ charging curve exhibits three states (positive pulse, no pulse, and negative pulse), where the zoomed-in area with a yellow background shows more detailed parts.

Fig. S9f illustrates the effect of the load resistance ($R$) on the current flowing through the load. When $R$ is too small, the output current shows a significant ripple. Additionally, as $R$ increases, the waveform of the current becomes stable. Since most electronic devices operate at approximately 1.5 V, Fig. 2h compares the time required to charge 1 mF and 3.3 mF capacitors to 1.5 V using an EMC *versus* a rectifier bridge. With only a rectifier bridge, charging the 1 mF capacitor to 1.5 V takes 226.6 s, while the 3.3 mF capacitor only reaches 0.67 V after 300 s. In contrast, under EMC management, the 1 mF capacitor reaches 1.5 V in just 23.4 s, and the 3.3 mF capacitor achieves the same voltage in 66.8 s. This represents charging-efficiency improvements of 94-fold and 134-fold, respectively.

## 2.3 Output performance of WFH-TENG under various parameters

The electrical performance of WFH-TENG for water flow energy harvesting is detailed in Fig. 3. Fig. 3a illustrates its working principle, which is based on the vertical motion of a pair of crown wheel structures. The lower crown wheel is rigidly connected to the blades *via* a steel shaft, while the upper crown wheel is constrained to vertical movement by a limiter. Water flow induces rotation in the nearly vertical blades, thereby rotating the lower crown wheel. The operational cycle consists of four stages, which are shown in Fig. 3a.

The vertical upward force on the crown gear ($F_{vertical}$) during ascent can also be derived by eqn (10), as follows: where $F_Q$ is the axial load of the upper crown gear, $G$ is the gravity force on the upper crown gear, $F_f$ is the friction on the blade, $m_{down}$ is the mass of the lower crown wheel and $m_{up}$ is the mass of the upper crown wheel. It can be seen that by increasing the water flow rate, the force received by the upper crown wheel will increase. This will shorten the rise time required for WFH-TENG, which means that the $I_{sc}$ will increase. WFH-TENG was tested at a water flow rate of 1.3 m s$^{-1}$ because the pump providing the water flow could not be adjusted for variable speed.

Given the 4 cm height of the crown wheel structure, the friction material achieves a maximum displacement of 4 cm relative to the electrode material in the separated state. To evaluate the impact of the electrode width, three widths were tested: 0.5 cm, 1 cm, and 2 cm. The influence of the electrode width on WFH-TENG output is analogous to the effect of the central electrode angle on the WH-TENG output.

Fig. 3b presents the relationship between $Q_{sc}$ and electrode width. Measurements, conducted using a 10 cm diameter cylinder over two complete motion cycles, show that changes in electrode width do not significantly affect $Q_{sc}$, which remains stable within the 120–135 nC range. However, as shown in Fig. 3c, the electrode width significantly influences the $I_{sc}$. Narrower electrodes facilitate charge transfer between multiple adjacent electrode pairs within a single rotation cycle, generating multiple current peaks. According to eqn (1), the total transferred charge per cycle remains constant. Therefore, a narrower electrode width delivers the same charge in a shorter effective transfer time, resulting in a higher peak current. Specifically, reducing the electrode width from 2 cm to 0.5 cm increased $I_{sc}$ from 1.72 μA to 5.75 μA. Given the stability of both $Q_{sc}$ and $I_{sc}$ at a 0.5 cm width, this value was selected for subsequent experiments.

For context, a 2 cm electrode width corresponds to half the crown wheel's height during its transition from the engaged (Fig. 3a-i) to the fully separated (Fig. 3a-ii) state. Under these conditions, a single set of reciprocal charge transfers occurs per cycle, yielding a single current peak (see detailed $Q_{sc}$ signal in Fig. S10a). The $I_{sc}$ exhibits a pronounced peak during the electrode's falling phase, driven by the work done by gravity. In contrast, the current during the rising phase is less

$$F_{vertical} = F_Q - G - F_f \sin \lambda$$

$$= \frac{F}{\tan(\lambda + \varphi)} - m_{up}g - \mu F_r \cdot \cos \varphi \cdot \sin \lambda$$

$$= \frac{1}{1 - \tan \varphi \cdot \cos \lambda \left( \frac{\cos \lambda}{\tan(\lambda + \varphi)} - \sin \lambda \right)} \cdot \left[ \frac{1}{\tan(\lambda + \varphi)} - \frac{\sin v(2\lambda)\tan \varphi}{2\tan(\lambda + \varphi)} + (\sin \lambda)^2 \tan \varphi \right] \cdot \frac{1}{2} \cdot \frac{\rho A C_d V^2 L}{\left( mL^2 + \frac{m_{down}r^2}{m} \right)} - m_{up}g \quad (10)$$

threaded contact surface, $\lambda$ is the angle of spiral rise, $F_r$ is the whole reaction force, $\mu$ is the dynamic friction factor, $\varphi$ is the angle between $F_r$ and $F_N$, $\rho$ is the density of water, $A$ is the projected area of the blade in the direction of vertical water flow, $C_d$ is the drag coefficient of the blade, $v$ is the flow velocity of water, $L$ is the radial length of the blade, $m$ is the total mass of

pronounced, as more time is required to overcome this gravitational work. Fig. S10b illustrates that the $V_{oc}$ remains largely unaffected by electrode width, stabilizing at approximately 350 V.

Fig. 3d and e present the output performance for cylinders of different diameters (8 cm, 10 cm, and 12 cm). While $Q_{sc}$ and $I_{sc}$
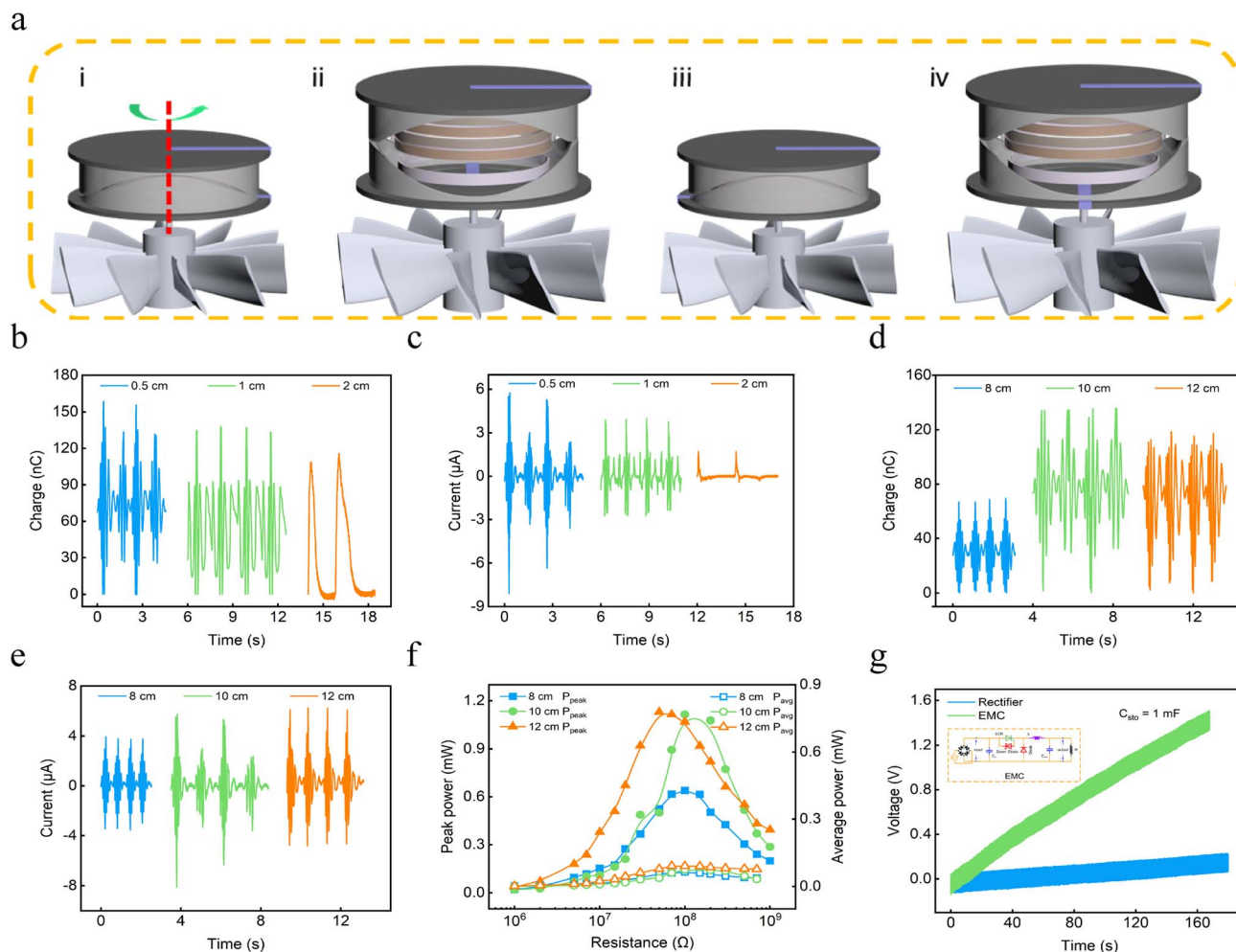
Fig. 3 Electrical test results of WFH-TENG. (a) Four operational phases within a single cycle of WFH-TENG. (b) Relationship between $Q_{sc}$ and electrode width. (c) Relationship between $I_{sc}$ and electrode width. (d and e) Output performance of the WFH-TENG units with varying cylinder diameters. (f) Peak power and average power of WFH-TENG at different electrode lengths. (g) Comparison of charging curves for a 1 mF capacitor using an EMC and rectifier bridge.

show consistent trends for the 8 cm and 12 cm cylinders, the data for the 10 cm cylinder are irregular. This anomaly is likely attributed to the limited 3D printing precision, which may have slightly compromised the interfacial contact between the FEP and Au layers, compared to the observations for the other two groups (Fig. S11). Overall, increasing the cylinder diameter expands the FEP-Au contact area, leading to enhanced output performance. Fig. 3f compares the output power of single cylinders with different diameters, revealing that larger diameters enhance both the average and peak powers while decreasing the matching impedance. This indicates that larger devices are better suited for powering sensors with low internal resistance.

To optimize the EMC, the voltage across the $C_{sto}$ was measured, as the stored energy is proportional to the square of this voltage (detailed results in Fig. S12a–c). As shown in Fig. 3g, the EMC circuit dramatically improves the capacitor charging efficiency, achieving a rate 46.5 times greater than that of a standard rectifier bridge. With the EMC circuit, WFH-TENG charged a 1 mF capacitor to 1.5 V in 180 s, whereas the rectifier bridge only reached 0.22 V in the same period.

## 2.4 Application of H-TENG

H-TENG offers the dual advantages of hybrid energy harvesting and straightforward fabrication. Its buoy-like shape facilitates simple deployment in marine environments, as illustrated in Fig. 4a. This system is designed to meet the power demands of Internet of Things (IoT) devices in offshore settings. IoT systems typically employ numerous sensors to monitor key environmental parameters, such as temperature, humidity, water level, and salinity. As a practical demonstration, Video S1 shows the operation of WH-TENG at a wind speed of 9 m s$^{-1}$, successfully powering two parallel thermo-hygrometers.

A 1 mF $C_{sto}$ was used as the energy storage unit, connected in parallel with the EMC circuit and the thermo-hygrometers. The selected thermo-hygrometer has a startup voltage of approximately 1.25 V and requires a sustained voltage above 1.5 V for normal operation. A conventional approach involves pre-charging $C_{sto}$ to 1.5 V before connecting the load to prevent
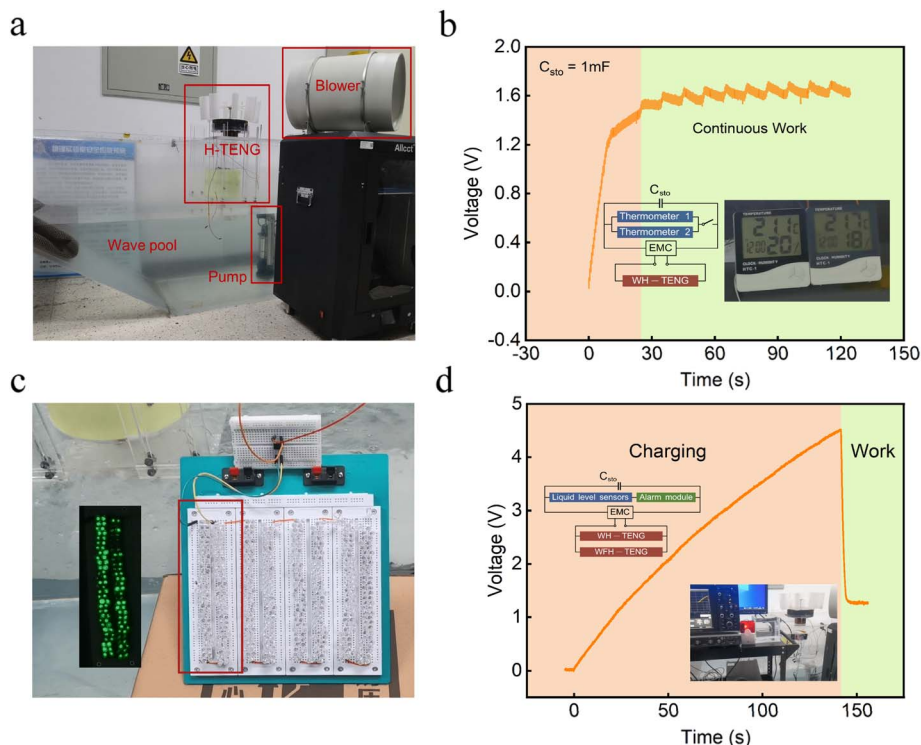
Fig. 4 Application demonstration of H-TENG. (a) Photograph of H-TENG being used as a drive power supply in a simulation test system. (b) Charging and working process of the capacitor when WH-TENG supplies power to thermo-hygrometers. (c) WFH-TENG powering 116 LEDs. (d) Charging and working process of the capacitor when H-TENG supplies power to a water-level alarm device.

repeated on-off cycles caused by insufficient instantaneous power. In contrast, our WH-TENG can power the thermo-hygrometer directly from the outset, eliminating the need for an initial charging phase and better simulating real-world application scenarios. As shown in Fig. 4b, which includes a circuit diagram, the voltage across $C_{sto}$ reaches the 1.55 V operating threshold in just 25.28 s. The TENG's high output ensures the voltage remains stable, enabling continuous, long-term operation of the sensor.

Beyond sensor operation, IoT systems may require visual displays. Fig. 4c demonstrates WFH-TENG's capacity to illuminate 116 series-connected LEDs (see Video S2 for the active circuit within the red frame). This output is sufficient to power a marine warning light capable of displaying simple text or signals. Finally, the complete H-TENG system was used to operate a water level alarm (Fig. 4d and Video S3). Given that the alarm's signal transmission module requires 4.5 V to activate, $C_{sto}$ was pre-charged. The initial charging time to 4.5 V was 141.6 s. Upon triggering the alarm at the water-level threshold, the voltage dropped sharply to approximately 1.27 V as the stored energy was discharged. For operation at a lower voltage of 3 V, the required H-TENG charging time was reduced to just 79 s.

## 3. Conclusion

In this study, we successfully designed and fabricated an H-TENG operating in freestanding mode. The device exhibited exceptional durability, maintaining 92% of its $Q_{sc}$ after seven weeks of continuous operation, attributed to the flexible contact between rabbit fur and a PTFE film. To enhance precision and efficiency, we employed 3D printing and EDA for all component fabrication, minimizing human error and shortening the production cycle. The constituent WF-TENG and WFH-TENG units generated peak currents of 15.16 μA and 6.24 μA, respectively, culminating in a total peak power output of 4.67 mW. Furthermore, an EMC was engineered to match the TENG's output characteristics. This integrated system continuously powers a thermo-hygrometer and rapidly activates a water-level alarm, enabling real-time monitoring of critical marine parameters like temperature, humidity, and water level. This work presents a viable solution for powering sensor networks through hybrid-energy harvesting, underscoring the significant potential of TENGs for sustainable, long-term marine energy harvesting.

## 4. Experimental section

### 4.1 Wind energy harvesting TENG preparation

WH-TENG consists of two main components: the TENG section, which includes a stator and rotor positioned at regular intervals, and the wind capture section, which features multiple wind cups mounted around a rotating axis. The rotor's acrylic substrate is supported by a ring of a 75 μm PI film, with intervals, and is covered with an 80 μm PTFE sponge. The stator is constructed using a 0.2 cm thick, 19 cm diameter rigid FR-4 sheet as the substrate, with a circular center angle of

approximately 15° copper as the electrode material. The two electrodes are spaced 2 mm apart and are coated with a 10 μm nylon layer to prevent dielectric breakdown due to high voltage between the electrodes. To reduce the resistance between the stator and rotor during rotation, three pieces of rabbit fur (7 cm long, 0.5 cm wide, and 0.4 cm high) are arranged at 120° intervals on the nylon surface. The wind cup and housing of WH-TENG are made from light-curing resin. The wind cup is designed as a half-hollow cylinder with a diameter of 6 cm and a height of 12 cm, while the housing shell is a hollow cylinder with a diameter of 20.5 cm. A 10 cm-long steel rod connects the flange rings fixed on both sides of the wind cup and rotor through a bearing. Horizontal airflow energy is converted into rotational energy through the wind cup. The spacing between the stator and rotor can be adjusted by turning the screws on the flange ring attached to the steel rod, ensuring that the rotor lightly touches the upper surface of the rabbit fur.

### 4.2 Water flow energy harvesting TENG preparation

WFH-TENG primarily consists of a TENG unit for power generation and a component for capturing water flow energy. The friction material of the TENG is in slight contact in order to achieve the highest possible output. Water flow energy is harnessed through a turbine with nearly vertical blades, engineered to capture the maximum amount of energy from the water flow. The separation between the rotor and stator is achieved using a crown wheel structure. This structure, along with the white cylinders that secure the film on both the rotor and stator, as well as the cylindrical housing, is fabricated using 3D light-curing resin printing technology. The rotor's acrylic substrate is equipped with half of a crown wheel for separation and three sets of hollow cylinders with diameters of 8 cm, 10 cm, and 12 cm, respectively. These cylinders are coated with a 50 μm-thick PI film, and an 80 μm-thick FEP film is applied at 0.5 cm intervals along their length. The acrylic substrate of the stator is fitted with the other half of the crown wheel and a corresponding set of three cylinders. A 0.07 mm-thick, 4.3 cm-wide printed circuit board and a flexible printed circuit board serve as the substrate, which is affixed to the columns. Au with a width of 4.4 mm was used as the electrode on the circuit board, and the distance between the two electrodes was 0.6 mm to prevent breakdown of the adjacent electrodes due to high voltage. The turbine blade has a diameter of 21 cm and a height of 7.2 cm, while the cylindrical housing has a diameter of 20.6 cm and a height of 16 cm. A bearing is fixed at the center of the acrylic plate at the bottom. A 15 cm long steel rod connects the stator and rotor through two flange rings, facilitating the transfer of water flow energy from outside the barrel to drive the operation of WFH-TENG.

### 4.3 Experimental measurements

A Keithley 6517B system electrometer was utilized to measure the $I_{sc}$ and $Q_{sc}$ of the TENG. The voltage of the TENG and EMC was measured using a digital oscilloscope (LeCroy WaveRunner 610Zi). An adjustable-speed ducted fan was employed to simulate air flow at varying wind speeds, while a low-power pump was used to replicate water flow in the wave pool. A porous cushion served as a wave absorber to reduce the effects of backflow.

## Author contributions

Jiaxi Hu: conceptualization, formal analysis, investigation, data curation, writing – original draft. Mengfan Li: methodology, formal analysis. Weiqi Cui, Jiaodi Li and Qiuxiang Wang: methodology. Ying Lou: writing – review and editing. Aifang Yu: supervision, writing – review and editing. Junyi Zhai: resources, supervision, funding acquisition, writing – review and editing. All authors gave final approval for publication.

## Conflicts of interest

The authors declare no conflict of interest.

## Data availability

The data supporting this article have been included as part of the supplementary information (SI). Supplementary information: key parameters of various reported works and this work, the video of powering thermo-hygrometers by WH-TENG, the video of powering LEDs by WFH-TENG, and the video of powering a water level alarm by H-TENG. See DOI: **https://doi.org/10.1039/d5se01144b**.

## Acknowledgements

## References

1 E. Sala, J. Mayorga, D. Bradley, R. B. Cabral, T. B. Atwood, A. Auber, W. Cheung, C. Costello, F. Ferretti, A. M. Friedlander, S. D. Gaines, C. Garilao, W. Goodell, B. S. Halpern, A. Hinson, K. Kaschner, K. Kesner-Reyes, F. Leprieur, J. McGowan, L. E. Morgan, D. Mouillot, J. Palacios-Abrantes, H. P. Possingham, K. D. Rechberger, B. Worm and J. Lubchenco, *Nature*, 2021, **592**, 397–402.
2 E. B. Barbier, *Ecosyst. Serv.*, 2015, **11**, 32–38.
3 G. Zhang, P. Yang, S. He, Y. Zheng and G. Song, *Mech. Syst. Signal Process.*, 2021, **147**, 107111.
4 I. H. Anchustegui and V. S. S. Radovich, *Energies*, 2022, **15**, 9157.
5 L. Cui, S. Amani, M. Gabr, W. G. P. Kumari, A. Ahmed, H. Ozcan, B. A. Horri and S. Bhattacharya, *Energies*, 2024, **17**, 1240.
6 S. Oliveira-Pinto and J. Stokkermans, *Proc. Inst. Civ. Eng. Marit. Eng.*, 2020, **173**, 120–135.
7 M. Lopez, N. Rodriguez and G. Iglesias, *J. Mar. Sci. Eng.*, 2020, **8**, 576.

8  H. P. Hanson, *Ocean. Eng.*, 2014, **87**, 78–83.

9  K. Shirasawa, K. Tokunaga, H. Iwashita and T. Shintake, *Renew. Energy*, 2016, **91**, 189–195.

10  F. L. Ponta and P. M. Jacovkis, *Renew. Energy*, 2008, **33**, 665–673.

11  M. L. Plummer and B. E. Feist, *Coast. Manag.*, 2016, **44**, 464–485.

12  R. Xu, H. Wang, Z. Xi, W. Wang and M. Xu, *J. Mar. Sci. Eng.*, 2022, **10**, 566.

13  F.-R. Fan, Z.-Q. Tian and Z. L. Wang, *Nano Energy*, 2012, **1**, 328–334.

14  X. Fu, S. Xu, Y. Gao, X. Zhang, G. Liu, H. Zhou, Y. Lv, C. Zhang and Z. L. Wang, *ACS Energy Lett.*, 2021, **6**, 2343–2350.

15  C. Ye, K. Dong, J. An, J. Yi, X. Peng, C. Ning and Z. L. Wang, *ACS Energy Lett.*, 2021, **6**, 1443–1452.

16  C. Zhang, Y. Liu, B. Zhang, O. Yang, W. Yuan, L. He, X. Wei, J. Wang and Z. L. Wang, *ACS Energy Lett.*, 2021, **6**, 1490–1499.

17  W. Zhang, Y. Gui, Y. Yang and C. Tang, *J. Clean. Prod.*, 2023, **429**, 139550.

18  Y. Gui, Y. Wang, S. He and J. Yang, *Energy Convers. Manage.*, 2022, **269**, 116098.

19  Z. Wang, Y. Wu, W. Jiang, Q. Liu, X. Wang, J. Zhang, Z. Zhou, H. Zheng, Z. Wang and Z. L. Wang, *Adv. Funct. Mater.*, 2021, **31**, 2103081.

20  G. M. Rani, C.-M. Wu, K. G. Motora, R. Umapathi and C. R. M. Jose, *Nano Energy*, 2023, **108**, 108211.

21  C. Zhang, W. Yuan, B. Zhang, J. Yang, Y. Hu, L. He, X. Zhao, X. Li, Z. L. Wang and J. Wang, *Small*, 2023, **19**, 2304412.

22  Y. Pang, Y. Fang, J. Su, H. Wang, Y. Tan and C. Cao, *Adv. Mater. Technol.*, 2023, **8**, 2201246.

23  J. Zhu, Y. Zeng, Y. Luo, Y. Jie, F. Lan, J. Yang, Z. L. Wang and X. Cao, *ACS Nano*, 2022, **16**, 11884–11891.

24  S. Cho, Y. Yun, S. Jang, Y. Ra, J. H. Choi, H. J. Hwang, D. Choi and D. Choi, *Nano Energy*, 2020, **71**, 104584.

25  L. Long, W. Liu, Z. Wang, W. He, G. Li, Q. Tang, H. Guo, X. Pu, Y. Liu and C. Hu, *Nat. Commun.*, 2021, **12**, 4689.

26  Y. Gui, W. Zhang, S. Liu, Y. Li, J. Yang, G. Jin, H. Huang, P. Yang and M. Gao, *Nano Energy*, 2024, **124**, 109498.

27  S. He, Y. Gui, Y. Wang, L. Cao, G. He and C. Tang, *ACS Sens.*, 2024, **9**, 1188–1198.

28  Y. Wang, Y. Gui, S. He and J. Yang, *Sens. Actuators, B*, 2023, **377**, 133053.

29  S. He, Y. Gui, Y. Wang and J. Yang, *Nano Energy*, 2023, **107**, 108132.

30  P. Cheng, H. Guo, Z. Wen, C. Zhang, X. Yin, X. Li, D. Liu, W. Song, X. Sun, J. Wang and Z. L. Wang, *Nano Energy*, 2019, **57**, 432–439.

31  J. Yan, N. Mei, D. Zhang, Y. Zhong and C. Wang, *Front. Energy Res.*, 2022, **10**, 966567.

32  Z. Qu, M. Huang, C. Chen, Y. An, H. Liu, Q. Zhang, X. Wang, Y. Liu, W. Yin and X. Li, *Adv. Funct. Mater.*, 2022, **32**, 2202048.

33  Y. Xu, W. Yang, X. Lu, Y. Yang, J. Li, J. Wen, T. Cheng and Z. L. Wang, *ACS Nano*, 2021, **15**, 16368–16375.

34  Y. Xi, H. Guo, Y. Zi, X. Li, J. Wang, J. Deng, S. Li, C. Hu, X. Cao and Z. L. Wang, *Adv. Energy Mater.*, 2017, **7**, 1602397.

35  G. Li, J. Wang, S. Fu, C. Shan, H. Wu, S. An, Y. Du, W. He, Z. Wang, W. Liu, Y. Nie, S. Liu, P. Wang and C. Hu, *Adv. Funct. Mater.*, 2023, **33**, 2213893.

36  H. Wu, S. Fu, W. He, C. Shan, J. Wang, Y. Du, S. Du, B. Li and C. Hu, *Adv. Funct. Mater.*, 2022, **32**, 2203884.

37  H. Wu, W. He, C. Shan, Z. Wang, S. Fu, Q. Tang, H. Guo, Y. Du, W. Liu and C. Hu, *Adv. Mater.*, 2022, **34**, 2109918.